LETTER

doi:10.1038/nature12635

Directional tissue migration through a self-generated chemokine gradient

Erika Donà[1], Joseph D. Barry[1], Guillaume Valentin[1]†, Charlotte Quirin[1], Anton Khmelinskii[2], Andreas Kunze[1], Sevi Durdu[1], Lionel R. Newton[1], Ana Fernandez-Minan[1]†, Wolfgang Huber[1], Michael Knop[2] & Darren Gilmour[1]

The directed migration of cell collectives is a driving force of embryogenesis[1–3]. The predominant view in the field is that cells in embryos navigate along pre-patterned chemoattractant gradients[2]. One hypothetical way to free migrating collectives from the requirement of long-range gradients would be through the self-generation of local gradients that travel with them[4,5], a strategy that potentially allows self-determined directionality. However, a lack of tools for the visualization of endogenous guidance cues has prevented the demonstration of such self-generated gradients *in vivo*. Here we define the *in vivo* dynamics of one key guidance molecule, the chemokine Cxcl12a, by applying a fluorescent timer approach to measure ligand-triggered receptor turnover in living animals. Using the zebrafish lateral line primordium as a model, we show that migrating cell collectives can self-generate gradients of chemokine activity across their length via polarized receptor-mediated internalization. Finally, by engineering an external source of the atypical receptor Cxcr7 that moves with the primordium, we show that a self-generated gradient mechanism is sufficient to direct robust collective migration. This study thus provides, to our knowledge, the first *in vivo* proof for self-directed tissue migration through local shaping of an extracellular cue and provides a framework for investigating self-directed migration in many other contexts including cancer invasion[6].

The zebrafish lateral line primordium is a migrating collective of approximately 100 cells that deposits a series of mechanosensory organs along the main body axis[7] and whose route is defined by a stripe of the chemokine Cxcl12a (also known as Sdf1a)[8]. Previous genetic studies have shown that the primordium can follow the Cxcl12a stripe efficiently in both directions[9], excluding an instructive role for a pre-patterned chemokine gradient. Two 'self-generated gradient' hypotheses, whereby tissues sculpt directional gradients from uniform extrinsic guidance cues, have been proposed to explain this remarkable behaviour. First, Cxcl12a internalization by the guidance receptor Cxcr4b could generate a dynamic chemokine gradient at the tissue's leading edge, which in mathematical models is sufficient to drive forward migration[10]. Second, directional symmetry could be broken by internalization of Cxcl12a at the tissue's trailing edge by Cxcr7 (refs 4, 11), a receptor with known Cxcl12a sinking[12,13] and signalling[14,15] functions. However, a lack of tools for the visualization of endogenous guidance signal activity has prevented the validation of self-generated gradient models in any *in vivo* context.

We therefore established a novel readout of chemokine activity by measuring receptor turnover at the cell surface, a well-characterized cellular response to ligand binding[16], using a tandem fluorescent protein timer (tFT) approach[17]. To this aim, we tagged the zebrafish Cxcr4b receptor with a tFT consisting of the superfolder green fluorescent protein (sfGFP) coupled to the slower maturing red fluorescent protein TagRFP. The red/green fluorescence ratio at the plasma membrane, hereafter referred to as the 'lifetime ratio', provides a direct indicator of the age of protein populations, whereby newly synthesized proteins show only green fluorescence, with red fluorescence increasing progressively with protein age. As the rate of ligand-triggered internalization determines how long receptors reside at the cell surface, receptor lifetime ratios would be predicted to decrease as chemokine levels increase (Fig. 1a). We first tested the response of the lifetime reporter in early-stage zebrafish embryos injected with defined concentrations of *cxcl12a* mRNA. This revealed that Cxcr4b–tFT lifetime ratios at the plasma membrane progressively decreased over a range of *cxcl12a* levels (Fig. 1b, c). Transgenic expression of the Cxcr4b–tFT reporter from a bacterial artificial chromosome (BAC) containing Cxcr4b *cis*-regulatory sequences (*cxcr4b:cxcr4b-tFT*) recapitulated Cxcr4b expression pattern and completely rescued the lateral line migration defect in Cxcr4b-deficient embryos (Extended Data Fig. 1), confirming that Cxcr4b–tFT was fully functional. Whole-mount embryo imaging revealed that Cxcr4b–tFT lifetime ratios varied in different embryonic tissues (Fig. 1d). A heat-shock-induced pulse of ubiquitous Cxcl12a (*hsp70:cxcl12a*) led to strongly enhanced receptor internalization and reduced lifetime ratios (Fig. 1e, f and Supplementary Video 1), with both the Cxcr4b–tFT reporter and endogenous receptor being sent for lysosomal degradation (Extended Data Fig. 2). Together, these experiments demonstrate that the Cxcr4b–tFT provides a dynamic readout of Cxcl12a chemokine activity in living embryos.

The Cxcr4b–tFT reporter was then used to study the pattern of chemokine activity across the lateral line primordium. Spatially resolved lifetime profiles along the tissue front–rear axis revealed a clear gradient in Cxcr4b activity, with twofold higher Cxcr4b–tFT lifetime ratios in follower cells than cells of the leading domain (Fig. 2a, c and Extended Data Fig. 3). Consistently, anti-Cxcr4b immunostainings confirmed that endogenous receptor levels are reduced at the plasma membrane in leading cells (Extended Data Fig. 4). To rule out the possibility that the observed gradient in receptor age results from a higher transcription in the front, we measured lifetime ratios of a membrane-tethered version of the tFT reporter (mem-tFT) that does not respond to the chemokine. A gradient in lifetime ratio was non-detectable when mem-tFT was expressed under identical genetic control (Fig. 2b, d and Extended Data Fig. 5). We conclude that the Cxcr4b–tFT lifetime ratio gradient across the primordium results from graded chemokine-triggered receptor turnover. Furthermore, imaging of Cxcr4b–tFT lifetime ratios across the primordium during recovery from a pulse of uniform Cxcl12a chemokine expression revealed that the gradient in receptor turnover was re-established as the effect of the chemokine pulse subsided (Fig. 2e, f and Supplementary Video 2). These data are consistent with the proposal that the primordium can self-generate a front–rear chemokine activity gradient that it dynamically maintains through interaction with its environment.

The establishment of a method to visualize the chemokine activity across the migrating tissue allowed us to determine the role of the endogenous chemokine receptors in shaping this gradient (Fig. 3a). Genetic inactivation of *cxcr4b* (mutant allele *cxcr4b*^{t26035} (ref. 18)) decreased

[1]EMBL Heidelberg, Meyerhofstraße 1, 69117 Heidelberg, Germany. [2]Zentrum für Molekulare Biologie der Universität Heidelberg, Deutsches Krebsforschungszentrum, DKFZ–ZMBH Allianz, Im Neuenheimer Feld 282, 69120 Heidelberg, Germany. †Present addresses: CABD, Universidad Pablo de Olavide, Carretera de Utrera km1, 41013 Seville, Spain (A.F.-M.); MRC National Institute of Medical Research, The Ridgeway, Mill Hill, London NW7 1AA, UK (G.V.).

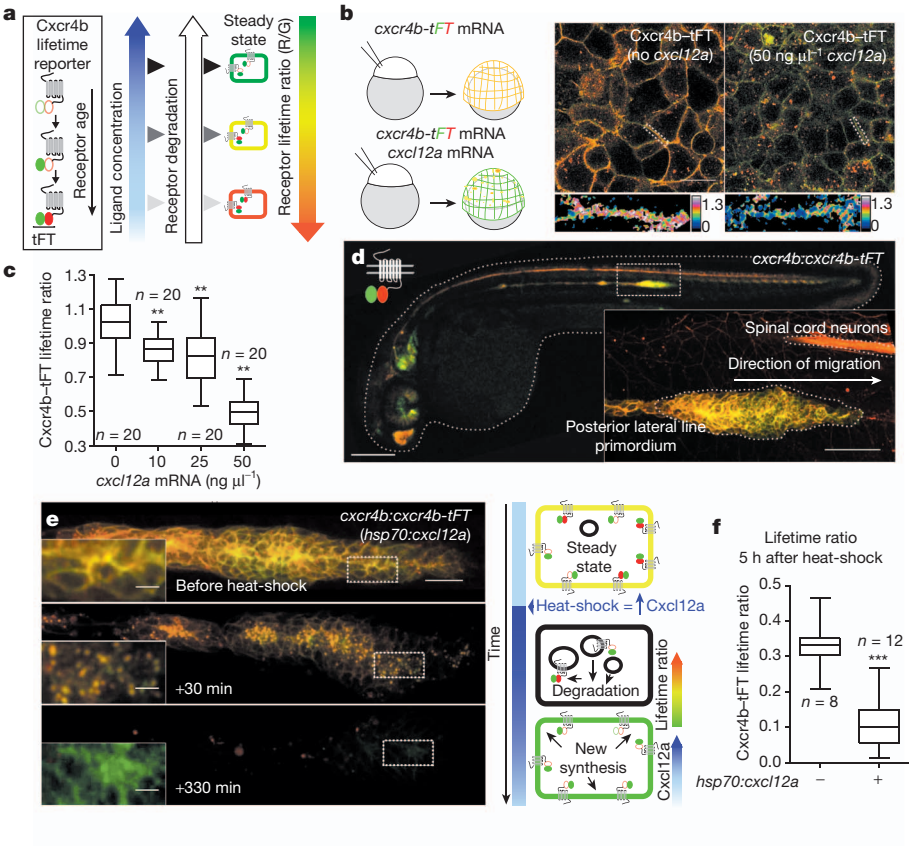

Figure 1 | Tandem fluorescent protein timers (tFTs) allow quantification of chemokine-dependent receptor turnover *in vivo*. **a**, Schema describing experimental rationale. Red/green intensity ratio increases as a function of protein age (left). Chemokine-dependent receptor-internalization rate determines ratio at plasma membrane (right). **b**, Top, schematic outline (left) and images of 7 h post-fertilization (h.p.f.) embryos injected with *cxcr4b-tFT* (middle) or *cxcr4b-tFT* plus *cxcl12a* mRNA (right), scale bar, 20 µm. Bottom, ratiometric images of squared areas (calibration bar = normalized red/green ratio). **c**, Box-and-whiskers plot of Cxcr4b–tFT lifetime ratios as a function of *cxcl12a* mRNA concentration (one-way analysis of variance (ANOVA) test with Dunnett's multiple comparison procedure; control group: 0 ng µl^{-1} *cxcl12a* mRNA; $^{**}P < 0.01$). **d**, BAC *cxcr4b:cxcr4b-tFT* embryo at 32 h.p.f. Inset, magnification of dashed area (scale bars: embryo, 200 µm; inset, 50 µm). **e**, Cxcr4b–tFT response to heat-shock-induced expression of Cxcl12a (*hsp70:cxcl12a*, Supplementary Video 1). Scale bars: primordium, 20 µm; insets, 5 µm. Insets, magnification of boxed areas (brightness increased in bottom inset for visualization). **f**, Tissue-scale Cxcr4b–tFT lifetime ratio 5 h after heat-shock in *hsp70:cxcl12a* and controls (heat-shock = 45 min, box-and-whiskers plot, Welch's *t*-test, $^{***}P < 0.001$). *n*, number of samples.

Cxcr4b–tFT lifetime ratios (Fig. 3c–e), indicating that the endogenous receptor reduces Cxcl12a levels available to the Cxcr4b–tFT reporter. Lifetime ratios were more strongly reduced in *cxcr7* mutants (*cxcr7*^{sa16} (ref. 19)), despite its expression being restricted to cells at the tissue rear (Fig. 3a–c). Conversely, knocking down *cxcl12a* in *cxcr7* mutants increased lifetime ratios to levels similar to *cxcl12a* null mutants (*cxcl12a*^{t30516} (ref. 20), Fig. 3c), confirming that the effect of Cxcr7 on Cxcr4b turnover is through regulating chemokine availability. Spatially resolved profiles revealed a pronounced reduction and flattening of Cxcr4b–tFT lifetime ratios in the rear two-thirds of *cxcr7* mutant primordia (Fig. 3b, e). Interestingly, Cxcr4b–tFT lifetime ratio was also decreased in the leading domain that does not express Cxcr7, consistent with the idea that Cxcr7 regulates Cxcl12a availability across the entire primordium (Fig. 3e, f). Direct testing of the Cxcr7 sink model came from expressing a fluorescently tagged version of Cxcl12a (Cxcl12a–GFP) in cells adjacent to the migrating primordium. Cxcl12a–GFP accumulated in cells at the rear of the tissue, in Cxcr7-positive endosomes (Fig. 3g, h, Supplementary Video 3 and Extended Data Fig. 6). Thus, although the extracellular chemokine gradient generated by the primordium cannot be directly visualized using currently available tools, this pattern of increased accumulation of Cxcl12a–GFP at the tissue rear probably represents a 'complementary image' of its extracellular distribution. We therefore conclude that Cxcr7 sink function at the tissue rear patterns chemokine activity across the migrating primordium.

We next determined whether the activity of these receptors as sinks for Cxcl12a is of functional importance during collective migration. To this aim, we compared the ability of wild-type and internalization-defective versions of Cxcr4b (Cxcr4b* (ref. 16)) and Cxcr7 (Cxcr7*, Extended Data Fig. 7) to alter primordium migration. We expressed each receptor form using a primordium-specific Gal4 line that drives

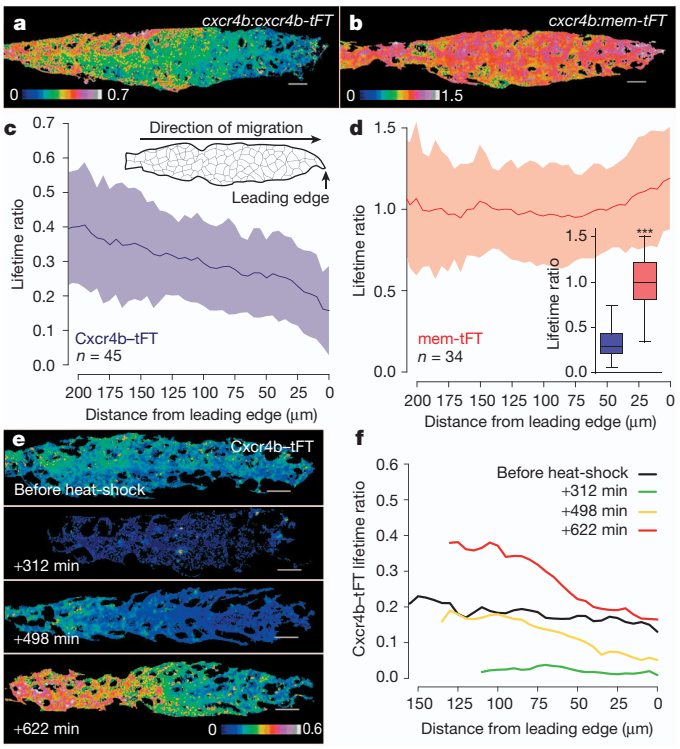

Figure 2 | Ligand-regulated chemokine receptor lifetime gradient indicates self-generated migration. **a**, **b**, Primordia expressing *cxcr4b:cxcr4b-tFT* (**a**) or a membrane-tethered version that does not respond to Cxcl12a (*cxcr4b:mem-tFT*) (**b**). **c**, **d**, Spatially resolved lifetime ratio profiles of Cxcr4b–tFT-expressing (**c**) and mem-tFT-expressing (**d**) primordia at 32 h.p.f. Inset, tissue-scale lifetime ratios (box-and-whiskers plot, Welch's *t*-test, $^{***}P < 0.001$). **e**, Cxcr4b–tFT ratiometric images after pulse of Cxcl12a (*hsp70:cxcl12a*, Supplementary Video 2). **f**, Quantification of images shown in **e**. Scale bars, 10 µm.

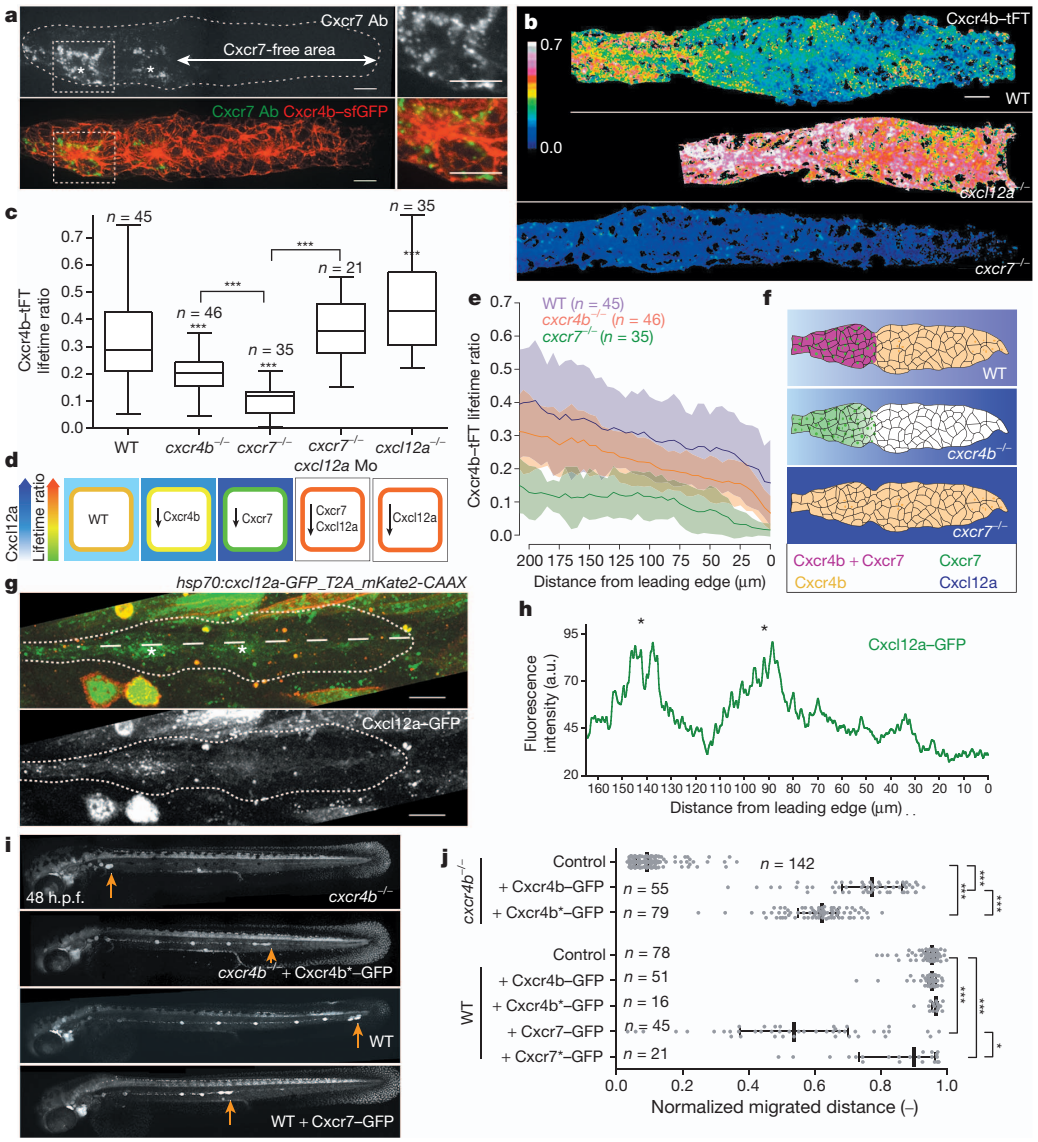

Figure 3 | Role of Cxcr4b and Cxcr7 sink activities in chemokine gradient formation. **a**, Expression pattern of Cxcr7 (anti-Cxcr7 antibody (Ab), green in bottom panel) and Cxcr4b (Cxcr4b–GFP, red in bottom panel). Cxcr7 vesicles cluster in apically constricted cells of organ progenitors (asterisks, insets). **b**, Ratiometric images of Cxcr4b–tFT primordia in wild type (WT, top), *cxcl12a*$^{-/-}$ (middle) and *cxcr7*$^{-/-}$ (bottom). Calibration bar shows the normalized red/green ratio. **c**, Box-and-whiskers plot of tissue-scale Cxcr4b–tFT lifetime ratios at 32 h.p.f. (Welch's *t*-test; asterisks refer to comparison with WT if not specified otherwise; ***$P < 0.001$). *cxcl12a* Mo, *cxcl12a* morpholino. **d**, Schematic interpretation of data in **c**. **e**, Spatially resolved Cxcr4b–tFT ratio profiles in WT (blue), *cxcr4b*$^{-/-}$ (orange) and *cxcr7*$^{-/-}$ (green). Line, median; shaded area, median absolute deviation (MAD). **f**, Schematic interpretation of data in **e**. **g**, **h**, Cxcl12a–GFP expressed outside primordium is internalized at tissue rear. **g**, Mosaic expression of *hsp70:cxcl12a-GFP_T2A_mKate2-CAAX* showing Cxcl12a–GFP distribution (green) and secreting cells (red) 1 h after heat-shock (maximum intensity projection, stack in Supplementary Video 3). **h**, Mean Cxcl12a–GFP intensities (along dashed line in **g**). **i**, Primordium migration (arrows) after Gal4/UAS expression of indicated receptor. **j**, Dot-plot, median and interquartile range of normalized distance migrated (one-way ANOVA test with Bonferroni's multiple comparison adjustment, *$P < 0.05$, **$P < 0.01$, ***$P < 0.001$). Scale bars, 10 μm (20 μm in **g**).

high-level expression in a mosaic pattern across the collective[21]. Overexpression of wild-type Cxcr4b–GFP had no influence on primordium migration and was able to rescue *cxcr4b* mutant primordia (Fig. 3j). Overexpression of Cxcr4b*–GFP gave similar results in both assays (Fig. 3i, j), demonstrating that Cxcr4b sink activity is dispensable for directional collective migration. By contrast, overexpression of wild-type Cxcr7–GFP markedly impaired migration (Fig. 3i, j) and caused elongation of the tissue (Extended Data Fig. 8), as expected from expanding the expression of a Cxcl12a sink within the primordium. By comparison, overexpression of Cxcr7*–GFP showed strongly reduced ability to interfere with migration (Fig. 3j), indicating that internalization is necessary for Cxcr7 activity in this context.

To test whether Cxcr7 sink activity is sufficient for migration, as predicted by the self-generated gradient model, we engineered an external source of Cxcr7 that followed the collective, achieved by expressing the receptor in the posterior lateral line nerve (pLLN) that extends under the primordium en route without influencing its movement[22] (Fig. 4a and Supplementary Video 4). Nerve expression of Cxcr7–GFP, achieved using a neural-specific promoter[23] (*nerve:cxcr7-GFP*) proved sufficient to interfere with the migration and morphology of wild-type primordia, with speed being reduced and the primordium becoming elongated (Fig. 4b, c and Supplementary Video 5). Interestingly, migration decelerated when the Cxcr7-expressing nerve advanced into the leading domain (Fig. 4c), indicating that the position of the Cxcr7 sink dynamically influences tissue behaviour. Moreover, *nerve:cxcr7–GFP* expression reinstalled directional migration in *cxcr7* mutant primordia with remarkable efficiency (Fig. 4d, e). Time-lapse imaging of these nerve-guided tissues again highlighted the importance of Cxcr7 sink positioning, with directional migration arresting when the nerve advanced into the leading domain and recommencing when it retracted to trailing regions (Fig. 4f, g and Supplementary Videos 6–8). Cxcr4b–tFT lifetime ratio analysis revealed a chemokine activity gradient across primordia in *nerve:cxcr7*-rescued embryos when compared to *cxcr7* mutant siblings, confirming that extrinsic Cxcr7 sink activity is sufficient to promote both directional migration and self-generated gradient formation (Fig. 4h–j).

The data presented here provide compelling experimental support for the idea that migrating collectives can determine their own directionality via a self-generated gradient mechanism. This has a number of implications for our understanding of cell movement in complex systems. Most obviously, autonomous dynamic remodelling of extracellular guidance cues by migrating tissues circumvents the necessity

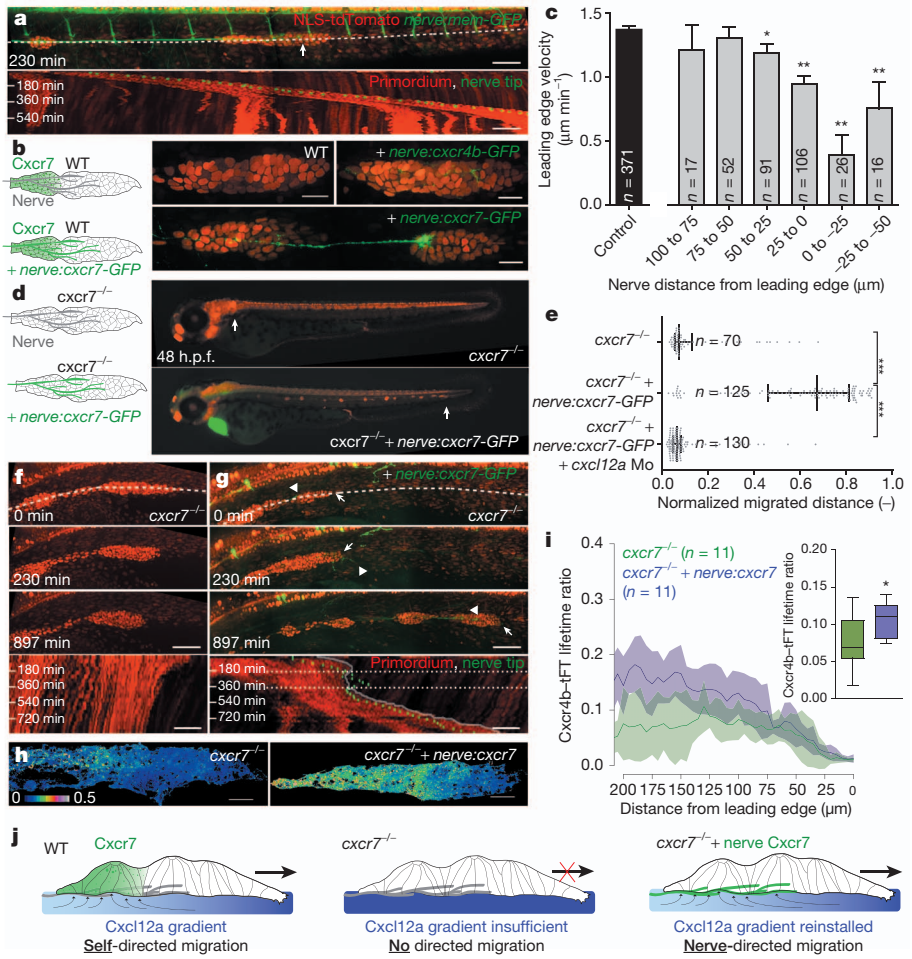

Figure 4 | Chemokine gradient formation by Cxcr7 drives collective migration. **a**, Still image of primordium (*cxcr4b:NLS-tdTomato*, red) and nerve (*nerve:mem-GFP*, green) at time-point 230 min of Supplementary Video 4, with kymograph (below). Arrow indicates nerve tip. **b**, Nerve-specific expression of Cxcr7–GFP (bottom), but not Cxcr4b–GFP (top right), alters primordium morphology (*cxcr4b:NLS-tdTomato*, red). **c**, Primordium leading-edge velocities as function of nerve distance (mean + s.e.m., one-way ANOVA test with Dunnett's multiple comparison procedure; $*P < 0.05$, $**P < 0.01$). **d**, **e**, Cxcl12a-dependent primordium migration rescue by nerve-specific expression of Cxcr7–GFP. **d**, Primordium migration (arrows) in $cxcr7^{-/-}$ (top), plus *nerve:cxcr7-GFP* (bottom). **e**, Dot-plot, median and interquartile range of normalized distance migrated (one-way ANOVA test with Bonferroni's multiple comparison adjustment, $***P < 0.001$). **f**, **g**, Time-lapse images of $cxcr7^{-/-}$ (**f**, Supplementary Video 6) and $cxcr7^{-/-}$ plus *nerve:cxcr7-GFP* (**g**, Supplementary Video 7) and corresponding kymographs (below). White dotted lines indicate nerve ahead of primordium. **h**, Ratiometric images of $cxcr7^{-/-}$ (left) and $cxcr7^{-/-}$ plus *nerve:cxcr7* primordia (right) at 28 h.p.f. **i**, Spatially resolved ratio profiles of $cxcr7^{-/-}$ (green) and $cxcr7^{-/-}$ plus *nerve:cxcr7* (blue) primordia at 28 h.p.f. Inset, tissue-scale lifetime ratios (box-and-whiskers plot, Welch's *t*-test; $*P = 0.012$). **j**, Model for nerve-rescue experiment. Scale bars, 20 μm (**b**, **h**), 50 μm (**a**, **f**, **g**).

for pre-existing long-range gradients, which may have spatial limitations. Moreover, it could coordinate the migration of multiple collectives within organisms, where gradients generated by one moving tissue accelerate or retard the migration of another. Our finding that the relocation of Cxcr7 allows the trailing nerve to direct the tissue that normally guides it shows that such higher-level coordination is possible. These experiments further show that signalling functions assigned to Cxcr7, such as β-arrestin recruitment[15], regulation of Cxcr4 expression[4] or heterodimerization with Cxcr4 (ref. 24), are dispensable for this process, thus providing further support for signalling-independent activities for Cxcr7 *in vivo*[12] and encouraging us to re-evaluate its role in lateral line migration[20] (Supplementary Discussion and Extended Data Fig. 9). Here we have used protein lifetime reporters to reveal an autonomously generated chemokine activity gradient across the axis of a migrating collective. Although a number of cellular mechanisms could influence receptor turnover rates across tissues[25], we demonstrate that Cxcr7 sink activity is required for and sufficient to pattern chemokine activity across the primordium. In the future it will be interesting to study how the tissue-scale chemokine gradient is converted to directed collective migration. For example, whether the self-generated gradient acts at the single-cell level, by directing the migration of individual cells within the leading domain, remains an open question. An attractive alternative, albeit non-mutually exclusive, proposal is that the function of Cxcr7 is to polarize motility at the tissue-scale by reducing chemokine activity levels to below a threshold, thus allowing follower cells behind the leading domain to adopt a different migratory behaviour. Finally, the generic nature of the lifetime imaging approach described here should facilitate the analysis of guidance signalling and self-generated gradient formation in other *in vivo* contexts. Given that Cxcr4 (ref. 26) and Cxcr7 (refs 27, 28) have important roles in cancer, it is tempting to speculate that a mechanism of this kind could promote the self-directed migration of tumour cells[6].

METHODS SUMMARY

Generation of Cxcr4b–tFT lifetime reporter BACs. Cxcr4b was tagged at the carboxy terminus with a TagRFP–sfGFP tFT through modification of the BAC clone CH211-145M5, containing 250 kilobases of genomic sequence, using standard ET recombineering technology[29] (Gene-Bridges).

Imaging of tFT reporter lines. Embryos were mounted in 1% low melting point (LMP) agarose in glass-bottom dishes (MatTek Corporation) and imaged on a Zeiss LSM 780 confocal microscope. High-resolution *z*-stacks of primordia were captured using a 63× water immersion objective (C-APOCHROMAT, 1.2 numerical aperture, Zeiss). Green and red signals were acquired sequentially using Gallium-Arsenide-Phosphide (GaAsP) detectors. A reference solution of purified mCherry–sfGFP fusion protein[17] was used to normalize for intensity fluctuations affecting the ratio. Low-resolution *z*-stacks of the entire embryo were acquired with a 20× objective (EL Plan-NEOFLUAR, 0.5 numerical aperture, Zeiss). Red and green images correspond to merged Gaussian filtered and flattened (sum projection) dual-colour *z*-stacks, whereas ratiometric images were generated from sum projections of segmented *z*-stacks. Colour-coding, if not specified otherwise, indicates red/green ratio after normalization by the reference solution.

Image analysis of lifetime ratios. Custom software written in R was used for automated data analysis, using many features of the open source R/Bioconductor image analysis package EBImage[30]. The complete image analysis code is available as part of the Bioconductor data package DonaPLLP2013 (http://www.bioconductor.org).

Statistical analysis. Statistical analysis of tissue-scale lifetime ratios was performed in R (Extended Data Fig. 10). The data set and vignette required to reproduce this analysis with runnable R code are available as part of the Bioconductor data package DonaPLLP2013 (http://www.bioconductor.org). GraphPad Prism 4.0 (GraphPad Software) was used for all other statistical analysis. Details of statistical tests are indicated in the figure legends. In box-and-whiskers plots the middle bar is the median, the hinges show the interquartile range (IQR) and the notches extend to ± 1.58 IQR/sqrt(*n*), where *n* is the number of samples.

Online Content Any additional Methods, Extended Data display items and Source Data are available in the online version of the paper; references unique to these sections appear only in the online paper.

Received 8 March; accepted 5 September 2013.
Published online 25 September 2013.

1. Friedl, P. & Gilmour, D. Collective cell migration in morphogenesis, regeneration and cancer. *Nature Rev. Mol. Cell Biol.* **10,** 445–457 (2009).
2. Rørth, P. Whence directionality: guidance mechanisms in solitary and collective cell migration. *Dev. Cell* **20,** 9–18 (2011).
3. Montell, D. J. Morphogenetic cell movements: diversity from modular mechanical properties. *Science* **322,** 1502–1505 (2008).
4. Dambly-Chaudière, C., Cubedo, N. & Ghysen, A. Control of cell migration in the development of the posterior lateral line: antagonistic interactions between the chemokine receptors CXCR4 and CXCR7/RDC1. *BMC Dev. Biol.* **7,** 23 (2007).
5. Scherber, C. *et al.* Epithelial cell guidance by self-generated EGF gradients. *Integr. Biol.* **4,** 259–269 (2012).
6. Friedl, P., Locker, J., Sahai, E. & Segall, J. E. Classifying collective cancer cell invasion. *Nature Cell Biol.* **14,** 777–783 (2012).
7. Ghysen, A. & Dambly-Chaudière, C. The lateral line microcosmos. *Genes Dev.* **21,** 2118–2130 (2007).
8. David, N. B. *et al.* Molecular basis of cell migration in the fish lateral line: role of the chemokine receptor CXCR4 and of its ligand, SDF1. *Proc. Natl Acad. Sci. USA* **99,** 16297–16302 (2002).
9. Haas, P. & Gilmour, D. Chemokine signaling mediates self-organizing tissue migration in the zebrafish lateral line. *Dev. Cell* **10,** 673–680 (2006).
10. Streichan, S. J., Valentin, G., Gilmour, D. & Hufnagel, L. Collective cell migration guided by dynamically maintained gradients. *Phys. Biol.* **8,** 045004 (2011).
11. Weijer, C. J. Collective cell migration in development. *J. Cell Sci.* **122,** 3215–3223 (2009).
12. Boldajipour, B. *et al.* Control of chemokine-guided cell migration by ligand sequestration. *Cell* **132,** 463–473 (2008).
13. Naumann, U. *et al.* CXCR7 functions as a scavenger for CXCL12 and CXCL11. *PLoS ONE* **5,** e9175 (2010).
14. Lee, E. *et al.* CXCR7 mediates SDF1-induced melanocyte migration. *Pigment Cell Melanoma. Res.* **26,** 58–66 (2013).
15. Rajagopal, S. *et al.* β-arrestin- but not G protein-mediated signaling by the 'decoy' receptor CXCR7. *Proc. Natl Acad. Sci. USA* **107,** 628–632 (2010).
16. Minina, S., Reichman-Fried, M. & Raz, E. Control of receptor internalization, signaling level, and precise arrival at the target in guided cell migration. *Curr. Biol.* **17,** 1164–1172 (2007).
17. Khmelinskii, A. *et al.* Tandem fluorescent protein timers for *in vivo* analysis of protein dynamics. *Nature Biotechnol.* **30,** 708–714 (2012).
18. Knaut, H., Werz, C. & Geisler, R. The Tübingen 2000 Screen Consortium & Nüsslein-Volhard, C. A zebrafish homologue of the chemokine receptor Cxcr4 is a germ-cell guidance receptor. *Nature* **421,** 279–282 (2003).
19. Kettleborough, R. N. W. *et al.* A systematic genome-wide analysis of zebrafish protein-coding gene function. *Nature* **496,** 494–497 (2013).
20. Valentin, G., Haas, P. & Gilmour, D. The chemokine SDF1a coordinates tissue migration through the spatially restricted activation of Cxcr7 and Cxcr4b. *Curr. Biol.* **17,** 1026–1031 (2007).
21. Distel, M., Wullimann, M. F. & Köster, R. W. Optimized Gal4 genetics for permanent gene expression mapping in zebrafish. *Proc. Natl Acad. Sci. USA* **106,** 13365–13370 (2009).
22. Gilmour, D., Knaut, H., Maischein, H.-M. & Nüsslein-Volhard, C. Towing of sensory axons by their migrating target cells *in vivo*. *Nature Neurosci.* **7,** 491–492 (2004).
23. Peri, F. & Nüsslein-Volhard, C. Live imaging of neuronal degradation by microglia reveals a role for v0-ATPase a1 in phagosomal fusion *in vivo*. *Cell* **133,** 916–927 (2008).
24. Levoye, A., Balabanian, K., Baleux, F., Bachelerie, F. & Lagane, B. CXCR7 heterodimerizes with CXCR4 and regulates CXCL12-mediated G protein signaling. *Blood* **113,** 6085–6093 (2009).
25. Nakayama, M. *et al.* Spatial regulation of VEGF receptor endocytosis in angiogenesis. *Nature Cell Biol.* **15,** 249–260 (2013).
26. Müller, A. *et al.* Involvement of chemokine receptors in breast cancer metastasis. *Nature* **410,** 50–56 (2001).
27. Hernandez, L., Magalhaes, M. A. O., Coniglio, S. J., Condeelis, J. S. & Segall, J. E. Opposing roles of CXCR4 and CXCR7 in breast cancer metastasis. *Breast Cancer Res.* **13,** R128 (2011).
28. Luker, K. E. *et al.* Scavenging of CXCL12 by CXCR7 promotes tumor growth and metastasis of CXCR4-positive breast cancer cells. *Oncogene* **31,** 4750–4758 (2012).
29. Zhang, Y., Muyrers, J. P., Testa, G. & Stewart, A. F. DNA cloning by homologous recombination in *Escherichia coli*. *Nature Biotechnol.* **18,** 1314–1317 (2000).
30. Pau, G., Fuchs, F., Sklyar, O., Boutros, M. & Huber, W. EBImage—an R package for image processing with applications to cellular phenotypes. *Bioinformatics* **26,** 979–981 (2010).

Supplementary Information is available in the online version of the paper.

Acknowledgements We are grateful to J. Ellenberg, F. Peri and S. De Renzis for comments on the manuscript, S. Streichan and the Gilmour laboratory for suggestions. We thank R. Koester and M. Distel for the lateral line Gal4-driver, E. Busch-Nentwich and D. Stemple for the *cxcr7* mutant identified by the Zebrafish Mutation Project, the European Molecular Biology Laboratory (EMBL) Monoclonal Antibody Facility for Cxcr7 and Cxcr4b antibodies, the EMBL Advanced Light Microscopy Facility for imaging assistance, B. Klaus from the EMBL Centre for Statistical Data Analysis for advice and A. Gruia for fish care. We acknowledge funding from the European Commission's FP7 Network of Excellence 'Systems Microscopy' (W.H. and J.D.B.), Marie Curie FP6 (A.F.-M.), European Molecular Biology Organization (A.Kh) and Deutsche Forschungsgemeinschaft SFB 488 (D.G.).

Author Contributions D.G. and E.D. designed study with input from M.K. and A.Kh. E.D. performed all experiments, C.Q. helped perform the nerve rescue experiments. J.D.B. and W.H. developed the data analysis methods. G.V. developed the BAC-complementation of Cxcr4b. A.Ku generated the *cxcr4b:NLS-tdTomato* line, S.D. generated the *UAS:cxcr7-GFP* line, L.R.N. designed and cloned the *hsp70:cxcl12a-GFP_T2A_mKate2-CAAX* construct, A.F.-M. designed and validated the Cxcr7 and Cxcr4b monoclonal antibodies. D.G. and E.D. wrote the paper with input from all authors.

Author Information Reprints and permissions information is available at www.nature.com/reprints. The authors declare no competing financial interests. Readers are welcome to comment on the online version of the paper. Correspondence and requests for materials should be addressed to D.G. (gilmour@embl.de).

METHODS

Zebrafish stocks. Zebrafish (*Danio rerio*) strains were maintained and staged as described previously[31]. Embryos were raised in E3 buffer at 30 °C, unless otherwise specified. The following mutant and transgenic strains were used: *cxcr4b*^{t26035} (ref. 18), *cxcl12a*^{t30516} (ref. 20), *cldnb:lyn–GFP*[9], *cxcr7*^{sa16} (ref. 19), *cxcr4a*^{um20} (ref. 32). *GAL4-UAS:mCherry* (ETL GA346) line was provided by R. Köster[21]. BAC transgenic lines are described below. Other transgenic lines were made using the Tol2kit[33]. All zebrafish experiments were conducted on embryos before 3 days post-fertilization, under the rules of the European Molecular Biology Laboratory and the guidelines of the European Commission, Directive 2010/63/EU.

mRNA synthesis and plasmids list. Capped mRNA was synthesized using mMessageMachine kit (Ambion). Used plasmids, generated as multisite-gateway clones (Invitrogen) using the Tol2kit[33], are listed below (in brackets the combined entry clones are indicated). 6×UAS promoter was provided kindly by R. Köster. Cxcr4b and Cxcr4b* constructs were a gift from the E. Raz laboratory (Cxcr4b* corresponds to construct 6 in ref. 16). Cxcr7* was created by removing the C-terminal 40 amino acids from Cxcr7 complementary DNA[20], following the strategy used in ref. 34 (Extended Data Fig. 7). Plasmids list is included here, where NBT = *Xenopus* neural-specific β-tubulin promoter[23] (corresponds to *nerve* promoter), mem = membrane tethering myristoylation sequence from Lyn kinase, T2A = viral 2A peptide, CAAX = CAAX prenylation sequence: SP6:Cxcr4b-TagRFP-sfGFP (p5′E(SP6/CMV)/pME(Cxcr4b noStop)/p3′E(TagRFP-sfGFP)), 6×UAS:Cxcr4b-GFP (p5′E(6xUAS)/pME(Cxcr4b noStop)/p3′E(GFP)), 6×UAS:Cxcr4b*-GFP (p5′E(6xUAS)/pME(Cxcr4b* noStop)/p3′E(GFP)), 6×UAS:Cxcr7-GFP (p5′E(6xUAS)/pME(Cxcr7 noStop)/p3′E(GFP)), 6×UAS:Cxcr7*-GFP (p5′E(6xUAS)/pME(Cxcr7* noStop)/p3′E(GFP)), hsp70:Cxcl12a (p5′E(hsp70)/pME(MCS)/p3′E(Cxcl12a)), nerve:Cxcr7-GFP (p5′E(NBT)/pME(Cxcr7 noStop)/p3′E(GFP)), nerve:Cxcr4b-GFP (p5′E(NBT)/pME(Cxcr4b noStop)/p3′E(GFP)), nerve:mem-GFP (p5′E(NBT)/pME(mem noStop)/p3′E(GFP)), nerve:Cxcr7 (p5′E(NBT)/pME(Cxcr7)/p3′E(polyA)), hsp70:Cxcl12a-GFP_T2A_mKate2-CAAX (p5′E(hsp70)/pME(Cxcl12a-GFP)/p3′E(T2A_mKate2-CAAX)).

BAC transgenesis. Four BACs were generated by modification of Cxcr4b BAC clone CH211-145M5 using the ET recombineering system[29] (Gene Bridges). The following selectable targeting cassettes were used for recombination. Targeting cassettes: (1) Lyn-tdTomato/late SV40 poly(A) signal/FRT-Kan^{R}-FRT; (2) TagRFP(noStop)-$(GlyAla)_5$-sfGFP/late SV40 poly(A) signal/FRT-Kan^{R}-FRT; (3) Lyn-TagRFP (noStop)-$(GlyAla)_5$-sfGFP/late SV40 poly(A) signal/FRT-Kan^{R}-FRT; (4) cry:CFP/Kan^{R}; (5) GFP/late SV40 poly(A) signal/FRT-Kan^{R}-FRT (in which cry = γ-crystallin promoter[33] and CFP = cyan fluorescent protein).

The following primers, encoding for left and right homology arms, were used to amplify the listed selectable targeting cassettes (indicated in brackets). The sequence homologous to the PCR template is underlined.

Forward primers (left homology arms): (1) 5′-GCGTGTCTCAGGGAACGGAGGACTATTTAAATGCTGCTGTGAGAGGAGGGCGGTTGACTGAAGTGTGGAGACTTATTGCGCCTTTTTGAGCGAGCCTCTAGAGCCACCATG-3′; (2) 5′-GATGCTGACCAAGAAAAGGGGGCCTATATCATCTGTATCTACTGAATCAGAGTCGTCCAGTGCACTGACGAGTATGGTGTCTAAGGGCGAAG-3′; (3) 5′-GCGTGTCTCAGGGAACGGAGGACTATTTAAATGCTGCTGTGAGAGGAGGGCGGTTGACTGAAGTGTGGAGACTTATTGCGCCTTTTTGAGCAAGTTTGTACAAAAAAGCAGGCT-3′; (4) 5′-CGCGGGGCATGACTATTGGCGCGCCGGATCGATCCTTAATTAAGTCTACTAATTATGATCCTCTAGATCAGATCT-3′; (5) 5′-TCCAGTCACAAGATGCTGACCAAGAAAAGGGGGCCTATATCATCTGTATCTACTGAATCAGAGTCGTCCAGTGCACTGACGAGTATGGTGAGCAAGGGCGAGGAG-3′.

Reverse primers (right homology arms): (1, 5) 5′-CATGATACACTTAAACTAGTCTTATTAATAATACTTATCAATGGAATGTCTGATAACACAGCGTTATAAATTAATCACAAGCCAACTTACCTAAAGGGAACAAAAGCTGGGTACC-3′; (2) 5′-ACACAAAAATACTTTACAATGTACAAAAACTGTAGTAAAGTCCTGTTTTTATAAGCTTAATCATCCATGTGGGCACCCGTGGCCGTATCT-3′; (3) 5′-CATGATACACTTAAACTAGTCTTATTAATAATACTTATCAATGGAATGTCTGATAACACAGCGTTATAAATTAATCACAAGCCAACTTACGCACCCGTGGCCGTATCT-3′; (4) 5′-GCGTAAGCGGGGCACATTTCATTACCTCTTTCTCCGCACCCGACATAGATATTACCCTGTTATCCCTAGAAACAGCTATGACCATGTAA-3′.

For *cxcr4b:NLS-tdTomato*, cassette 1 was inserted after *cxcr4b* first intron, leaving the first 5 amino acids encoded by the first exon, which when fused to the membrane-tethering myristoylation sequence from Lyn kinase gave rise to a nuclear localization sequence (NLS). *cxcr4b:cxcr4b-tFT* (receptor C-terminal fusion) and *cxcr4b:mem-tFT* (receptor transcriptional reporter, a tFT tethered to the membrane by the mem sequence) were generated in two steps. First, cassettes 2 and 3 were inserted to replace Cxcr4b STOP and ATG starting codons, respectively. Then, *cry:CFP* transgenic marker (cassette 4) was introduced into the pTARBAC2.1 backbone. For *cxcr4b:cxcr4b-GFP* (receptor C-terminal fusion) BAC line Cxcr4b STOP codon was replaced by cassette 5. FRT-flanked kanamycin-resistance cassette (FRT-Kan^{R}-FRT) was removed with FLP recombinase in all modified BACs. The inserted fragments and the regions flanking the recombination sites were sequenced before purification of positive clones (Large Construct Kit, Qiagen). Embryos were injected at one-cell stage, raised to adulthood and screened for fluorescence expression.

***cxcl12a* knockdown.** Previously described *cxcl12a* morpholino MO3 (ref. 12) (5′-CTACTACGATCACTTTGAGATCCAT-3′, Gene Tools) was diluted to 1 mM and injected at one-cell stage. Injection efficacy was monitored by scoring the number of arrested primordia in injected wild-type control embryos.

Analysis of Cxcr4b–tFT lifetime ratio in early embryos. *cxcr4b-tFT* mRNA (200 ng μl^{-1}, drop size ~0.6 nl) was injected alone or in the presence of titrating concentrations of *cxcl12a* mRNA (10, 25 and 50 ng μl^{-1}) in one-cell stage embryos. Dechorionated 7 h.p.f. embryos were mounted in 0.8% low melting point (LMP) agarose and high-resolution confocal images were acquired as described in the section 'Imaging of tFT reporters'. After background subtraction, membrane fragments were manually defined using the freehand line tool in Fiji (line width = 0.9 μm) followed by calculation of the mean red and green fluorescence intensities. Red/green ratios were normalized by the ratio of the sfGFP–mCherry reference solution and averaged per embryo. One embryo represents one data point.

Imaging of tFT reporters. Embryos were mounted in 1% LMP agarose in glass-bottom dishes (MatTek Corporation) and imaged on a Zeiss LSM 780 confocal microscope at 30 °C. High-resolution 16-bit *z*-stacks of primordia (pixel size = 0.131 μm, *z*-space = 0.5 or 1 μm) were captured using a 63× water immersion objective (C-APOCHROMAT, 1.2 NA, Zeiss). Green and red signals (green: ex. 488 nm, em. 489–550 nm; red: ex. 561 nm, em. 568–664 nm, A.U. = 1) were acquired sequentially by line using Gallium-Arsenide-Phosphide (GaAsP) detectors. A reference solution of purified mCherry–sfGFP fusion protein[17] was used to normalize for intensity fluctuations affecting the ratio. Low-resolution 16-bit *z*-stacks of the entire embryo (*z*-space = 10 μm, pixel size = 0.83 μm) were acquired with a 20× objective (EL Plan-NEOFLUAR, 0.5 NA, Zeiss). Red and green images correspond to merged Gaussian filtered and flattened (sum projection) dual colour *z*-stacks, whereas ratiometric images were generated as described in the section 'Generation of ratiometric images'.

Image analysis of lifetime ratios. The complete image analysis code is available as part of the Bioconductor data package DonaPLLP2013 (http://www.bioconductor.org). Blind sample selection was not possible, as mutant phenotypes were easily identifiable; however, specimens of each genotype were randomly selected from age-matched pools and lifetime ratios were extracted using an automated analysis pipeline, preventing bias in assessing the outcome of each experiment. In brief, *z*-stacks of primordia were acquired as described above and corrected for background. The green channel was chosen as the reference channel owing to the fast maturation kinetics of sfGFP and, from this, a binary mask of the primordium membrane (membrane–mask) was obtained by smoothing and adaptive thresholding. Then, a binary tissue–mask was computed and the axis of migration, along which all samples were aligned, was extracted using principal component analysis. Only pixels lying within the intersection of membrane–mask and tissue–mask (tissue–membrane–mask) were considered for subsequent calculations. To reduce the effects of pixel noise and chromatic aberration, a three-dimensional running median across the tissue (cube side-length of 10 μm) was computed in both channels. Red/green fluorescence intensity ratios were then calculated and normalized using a mCherry–sfGFP[17] reference solution acquired with the same imaging conditions. This procedure was necessary to compensate for day-to-day fluctuations of the instrument and permitted direct comparison of samples imaged on different sessions. To obtain tissue-scale lifetime ratios we calculated the median of normalized red/green fluorescence intensity ratios within the tissue–membrane–mask. Alternatively, to obtain spatially resolved lifetime ratio profiles, the median ratio along the axis of migration *x* (that is, through *yz*) was computed.

Generation of ratiometric images. From the image analysis we obtained background subtracted, Gaussian smoothed and membrane-masked *z*-stacks of the primordium in both red and green channels, which were further processed with Fiji. Stacks were flattened using sum projection, red/green ratio images were created using the Image Calculator plugin. These were then further normalized by dividing by the ratio of the reference solution. For visualization, images were colour-coded using the ratio lookup table in Fiji.

Statistical analysis. Statistical analysis of lifetime ratios was performed using R. The data set and vignette required to reproduce the analysis with runnable R code are available as part of the Bioconductor data package DonaPLLP2013 (http://www.bioconductor.org). To generate the analysed data set, consisting of normalized tissue-scale lifetime ratios obtained as described in the section 'Image analysis of lifetime ratios', embryos were carefully staged and always imaged at the same developmental stage (32 h.p.f.) to ensure comparability. Moreover, a calibration solution of purified mCherry–sfGFP fusion protein[17] was used to normalize for

variability in imaging conditions. As the effect size was not known a priori, we ran initial samples to obtain a first estimate of it. From these experiments we estimated that approximately $n > 20$ samples would be sufficient to obtain enough statistical power; however, we imaged sample sizes of up to $n = 46$, from at least three technical replicates per condition. Subsequent statistical testing demonstrated high statistical power owing to these large sample sizes. The distribution of all tissue-scale ratios is shown in Extended Data Fig. 10a, allowing inspection of the variation between samples. Consistency with assumptions of normal distribution of the data was assessed by generation of quantile-quantile (Q-Q) plots for each condition individually (Extended Data Fig. 10b). These indicated that the data were sufficiently close to being normally distributed, therefore two-sided Welch's *t*-tests for each of the comparisons of interest and multiple testing correction across these comparisons with Bonferroni's method were performed. An alternative, non-parametric test, the two-sided Mann–Whitney test (a two-sample Wilcoxon test), returned comparable results leading to the same biological interpretation of the data (Extended Data Fig. 10c).

GraphPad Prism 4.0 (GraphPad Software) was used for all other statistical analysis. Details of statistical tests are indicated in the figure legends. In box-and-whiskers plots the middle bar is the median, the hinges show the interquartile range (IQR) and the notches extend to $\pm$ 1.58 IQR/sqrt(n), where n is the number of samples.

Heat-shock induction of Cxcl12a. Embryos were raised and imaged at 28 °C to avoid leakage of the *hsp70* promoter and heat-shocked at 38 °C in a water bath for 30 min if not indicated otherwise. Imaging was performed as described in the section 'Imaging of tFT reporters'. For time-lapse experiments four tiles were acquired and the area corresponding to the primordium was manually defined for further analysis. A time interval of approximately 1 h was chosen to minimize photobleaching and allow multi-position acquisition.

Mosaic expression of Cxcl12a–GFP. Embryos were injected at one-cell stage with *hsp70:cxcl12a-GFP_T2A_mKate2-CAAX*, raised at 28 °C. 32 h.p.f. embryos were heat-shocked at 38 °C for 1 h, mounted as described and imaged on a Zeiss LSM 780 confocal microscope (63× objective, GaAsP detector, pixel size = 0.131 μm). Owing to low intensity of the GFP signal the pinhole was opened to 2 a.u. Stacks were flattened by maximum intensity projection for visualization and by sum projection to calculate mean fluorescence intensities across the primordium midline (line width = 7.2 μm).

Immunostaining. Whole-mount antibody staining was performed following standard procedures[31]. Monoclonal anti-Cxcr7 and anti-Cxcr4b (zebrafish) antibodies were generated by the EMBL Monoclonal Antibody Facility using the following peptides sequences as antigens: MSVNVNDFNDILDALGELNFC and MEFYDS IILDNSSDSGSGDYDGEELC, corresponding to the amino terminus of Cxcr7 and Cxcr4b receptors, respectively. Antibody specificity was confirmed by demonstrating a lack of immunostaining pattern in embryos mutant for the respective receptor. Rabbit-anti GFP (Torrey Pines Biolabs) was used for staining of Cxcl12a–GFP. Goat anti-mouse Alexa Fluor 647 and goat anti-rabbit Alexa Fluor 488 (Molecular Probes) were used as secondary antibodies. Imaging was performed on either a Zeiss LSM 780 confocal microscope as described or a PerkinElmer Improvision Ultraview VoX Spinning disk confocal. In this case, a 63× water immersion objective (C-APOCHROMAT, 1.2 NA, Zeiss, pixel size = 0.106 μm, z-space = 0.5 μm) and the following imaging settings were used: sequential acquisition; dichroic: multi pass 405/488/568/640; green: ex. 488 nm, em. single BP 525(W50); far red: ex. 640 nm, em. double BP 485(W60), 705(W90). Images were smoothed by Gaussian filter and flattened using maximum intensity projection in Fiji.

Time-lapse imaging and primordium migration analysis. Time-lapse experiments for the analysis of primordium migration were carried out at 30 °C on a PerkinElmer Improvision Ultraview VoX Spinning disk confocal using 25× multi-immersion objective (Plan-APOCHROMAT, 0.8 NA, Zeiss). Image analysis was performed in Fiji. z-stacks spanning the whole primordium (z-space = 1 μm) were flattened by maximum intensity projection and stitched using the Pairwise Stitching plugin[35] where necessary. Kymographs were generated using the Kymograph plugin (line width = 2 μm). When GFP fluorescent nerve was present, the furthermost axon growth cone was manually indicated with a point on the migration path before creating the kymograph.

Time-lapses for the analysis of primordium migration speed (Fig. 4c) were 3–5 h long (time interval = 10 min). Primordium and nerve tips were tracked using the Manual Tracking plugin. Primordium tip instantaneous velocities were extracted (directionality: plus = anterior to posterior, minus = posterior to anterior) and binned depending on the distance between the tip of Cxcr7–GFP-positive nerve and the leading edge of the primordium at that time-point (binning window = 25 μm). A minus sign was assigned to the distance when the nerve tip was in front of the primordium. Sixteen movies per condition (wild type or wild type plus nerve:Cxcr7) were analysed.

Overviews of 48 h.p.f. embryos were acquired using a Leica MZ16F fluorescence stereomicroscope. Distances from the ear to the primordium and from the ear to the tail of the fish were measured using Fiji and their ratio was calculated.

LysoTracker Red DND-99 staining. Dechorionated embryos were incubated for 90 min in 1 μM LysoTracker Red DND-99 dye (Molecular Probes) in fish E3 medium plus 1% dimethylsulphoxide (DMSO).

Bafilomycin A1 Inhibition of lysosomal function. Dechorionated embryos were incubated in E3 medium plus Bafilomycin A1 (Sigma) at a final concentration of 300 nM for 3 h or 3 μM for 40 min. Embryos were then either fixed in 4% paraformaldehyde or mounted in 1% LMP agarose and imaged immediately.

Quantification of endogenous Cxcr4b degradation in response to Cxcl12a overexpression. *cldnb:lyn-GFP/hsp70:cxcl12a* double-transgenic embryos were heat-shocked for 1 h at 38 °C and subsequently incubated for 3 h in the presence of Bafilomycin A1 at a final concentration of 300 nM or 0.01% DMSO (control). Control embryos (*cldnb:lyn-GFP* without *hsp70:cxcl12a*) were also heat-shocked. Embryos were then fixed in 4% paraformaldehyde and stained for Cxcr4b using the described monoclonal anti-Cxcr4b antibody. z-stacks spanning the whole primordium were acquired on a Zeiss LSM 780 confocal microscope. After background subtraction (rolling ball algorithm in Fiji) images were flattened using sum projection and Cxcr4b total fluorescence intensity was calculated within a primordium mask defined using the Lyn–GFP counter-label.

Analysis of Cxcr4b distribution across the primordium. *cldnb:lyn-GFP* transgenic embryos were fixed at 32 h.p.f. and stained for Cxcr4b using the afore mentioned monoclonal anti-Cxcr4b antibody. Confocal stacks were acquired on a Zeiss LSM 780 as already described for tFT reporters imaging. The same pipeline used for the ratiometric analysis of Cxcr4b–tFT was followed, with two differences: the intersection of the green and red individual masks was used as membrane mask and profiles were normalized by mean ratio in the front 15 μm of the tissue.

Cxcr4a's role in primordium migration. Whole-mount *in situ* hybridization of Cxcr4a was performed using standard procedures. Cxcr4a probe and *cxcr4a*^{um20} (ref. 32) were provided by A.F. Siekmann. *cxcr4b:NLS-tdTomato/cxcr4a*$^{um20/+}$ transgenic fish were in-crossed and primordium migration analysis was performed as already described.

31. Westerfield, M. *The Zebrafish Book: A Guide for the Laboratory use of Zebrafish (Brachydanio rerio)* 2nd edn (University of Oregon Press, 1993).
32. Siekmann, A. F., Standley, C., Fogarty, K. E., Wolfe, S. A. & Lawson, N. D. Chemokine signaling guides regional patterning of the first embryonic artery. *Genes Dev.* **23,** 2272–2277 (2009).
33. Kwan, K. M. *et al.* The Tol2kit: a multisite gateway-based construction kit for Tol2 transposon transgenesis constructs. *Dev. Dyn.* **236,** 3088–3099 (2007).
34. Canals, M. *et al.* Ubiquitination of CXCR7 controls receptor trafficking. *PLoS ONE* **7,** e34192 (2012).
35. Preibisch, S., Saalfeld, S. & Tomancak, P. Globally optimal stitching of tiled 3D microscopic image acquisitions. *Bioinformatics* **25,** 1463–1465 (2009).

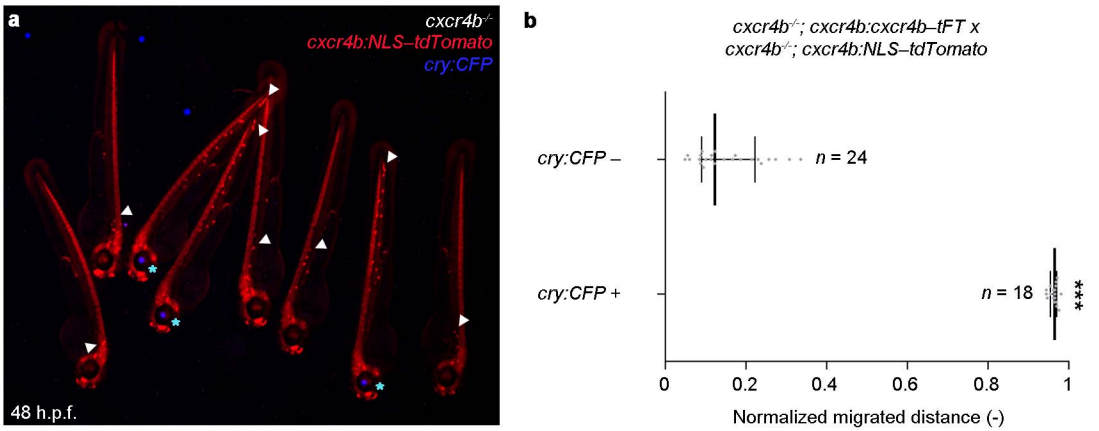

Extended Data Figure 1 | *cxcr4b:cxcr4b-tFT* BAC rescues primordium migration defect in *cxcr4b* mutants. **a**, Image of *cxcr4b* mutant embryos, where primordium migration (white arrowheads) is made visible by *cxcr4b:NLS-tdTomato* (red). Fish carrying *cxcr4b:cxcr4b-tFT* transgenes are identifiable by an independent transgenic marker that labels the lens blue (*cry:CFP*, asterisks). **b**, In all *cxcr4b:cxcr4b-tFT* transgenic embryos the primordium migrated normally, whereas non-transgenics showed migration defects typical of *cxcr4b* mutants[20]. Dot-plot, median and interquartile range of the indicated number of samples are shown (Welch's *t*-test, $***P < 0.0001$).

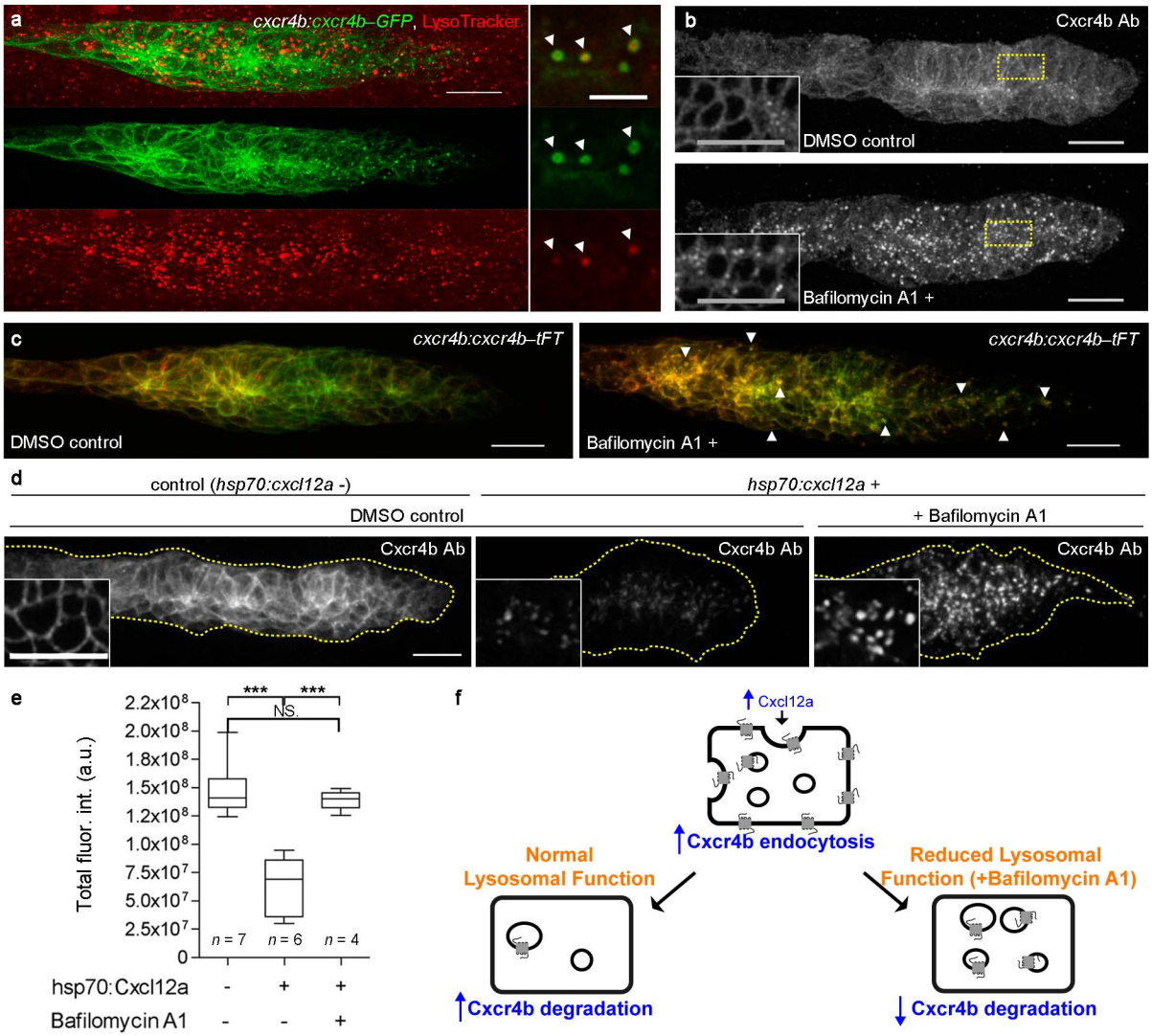

Extended Data Figure 2 | Cxcl12a-induced internalization targets Cxcr4b to lysosomal degradation. **a**–**c**, Cxcr4b is sent for lysosomal degradation in wild-type embryos. **a**, *cxcr4b:cxcr4b-GFP* embryo stained with the lysosomal marker LysoTracker Red DND-99. Left, maximum intensity projection of a primordium confocal *z*-stack (scale bar, 20 μm) showing Cxcr4b–GFP (green) and LysoTracker (red) localization. Right, magnification of single confocal plane showing LysoTracker and Cxcr4b–GFP co-localization (arrowheads; scale bar, 5 μm). **b**, Impaired lysosomal acidification leads to accumulation of endogenous Cxcr4b in intracellular vesicles. Anti-Cxcr4b (maximum intensity projections) of Bafilomycin A1-treated embryos (bottom) and controls (top; DMSO (dimethylsulphoxide)). **c**, Bafilomycin A1 treatment results in an increased number of Cxcr4b–tFT vesicles. Images show maximum intensity projections of *z*-stacks (scale bar, 20 μm). **d**–**f**, High Cxcl12a levels cause increased degradation of endogenous Cxcr4b. **d**, Anti-Cxcr4b immunohistochemistry 3 h after heat-shock induction (1 h at 38 °C) of *hsp70:cxcl12a* (sum projection of confocal *z*-stacks). **e**, Quantification of Cxcr4b levels within the primordium (box–and–whiskers plot, one-way ANOVA test with Bonferroni's multiple comparison adjustment, $***P < 0.001$) showing significantly reduced levels in *hsp70:cxcl12a* transgenics compared to non-transgenic controls. This effect is suppressed by Bafilomycin A1 treatment, resulting in increased accumulation of Cxcr4b-positive intracellular vesicles (**f**). Insets show single plane magnification of the squared area. Scale bars, 20 μm. NS, not significant.

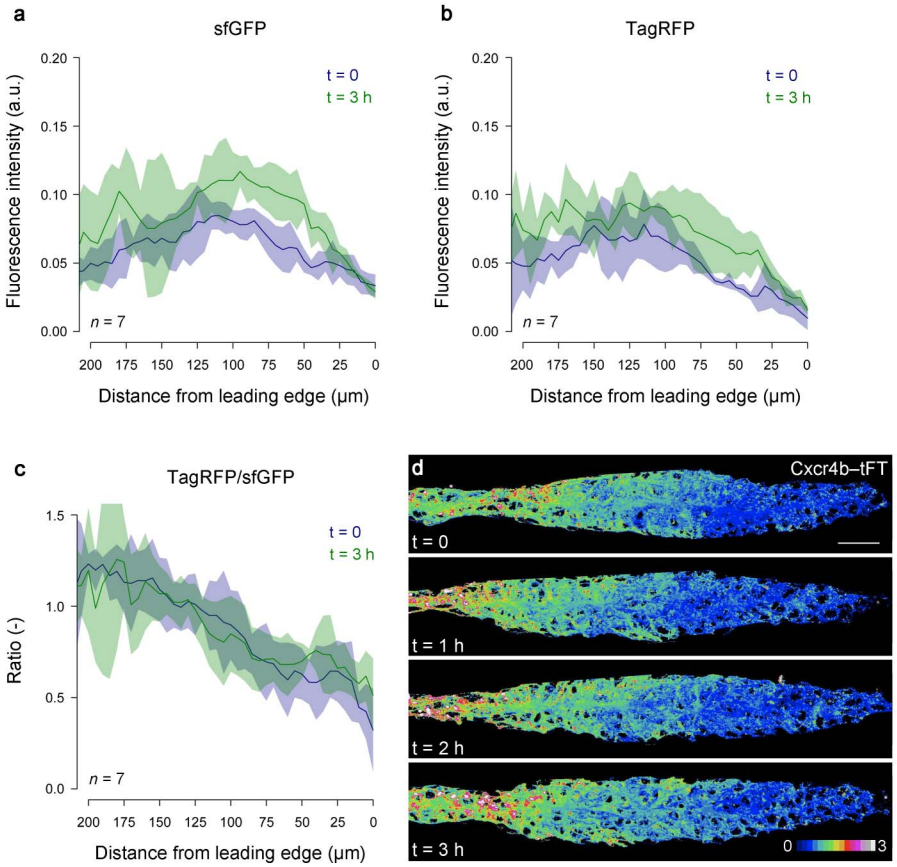

Extended Data Figure 3 | Cxcr4b–tFT lifetime ratio is stable over several hours. **a**–**c**, Spatially resolved profiles of Cxcr4b–tFT-expressing primordia at 32 h.p.f. ($t = 0$) and 35 h.p.f. ($t = 3$ h) show that although sfGFP (**a**) and TagRFP (**b**) median fluorescence intensities increase through time, their ratio instead stays constant and maintains a gradient across the front–rear axis of the tissue (**c**). Median and MAD of 7 samples acquired on the same day with identical imaging conditions are shown. **d**, Ratiometric images of one representative sample through time. Lookup table = red/green fluorescence intensity ratio. Scale bar, 20 μm. All lifetime measurements were performed during this time window, whenever possible.

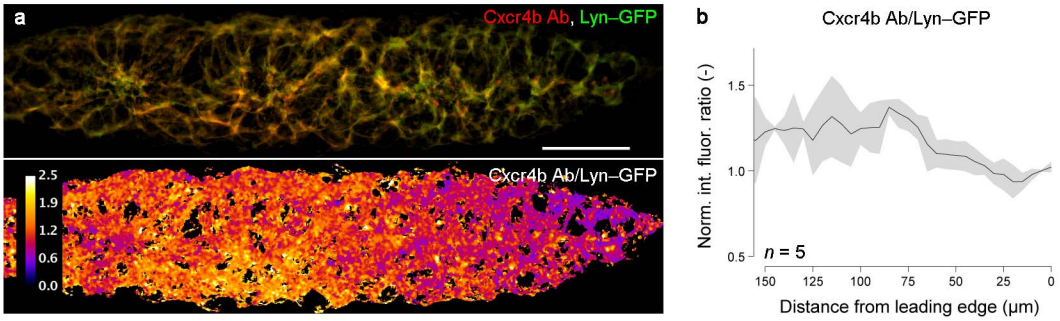

Extended Data Figure 4 | Increased turnover in primordium leading domain results in graded distribution of endogenous Cxcr4b receptor. Anti-Cxcr4b immunohistochemistry reveals a gradient of endogenous receptor along the primordium. **a**, Cxcr4b antibody (red) and a homogeneous membrane counter-label given by *cldnb:lyn–GFP* transgenic line (green) displayed in segmented (top, sum projection of segmented stack) and ratiometric form (bottom, calibration bar = Cxcr4b antibody/Lyn–GFP fluorescence intensity ratio). **b**, Cxcr4b antibody/Lyn–GFP fluorescence intensity ratio profiles. Median and MAD after normalization of individual profiles by the front-most 15 μm are plotted.

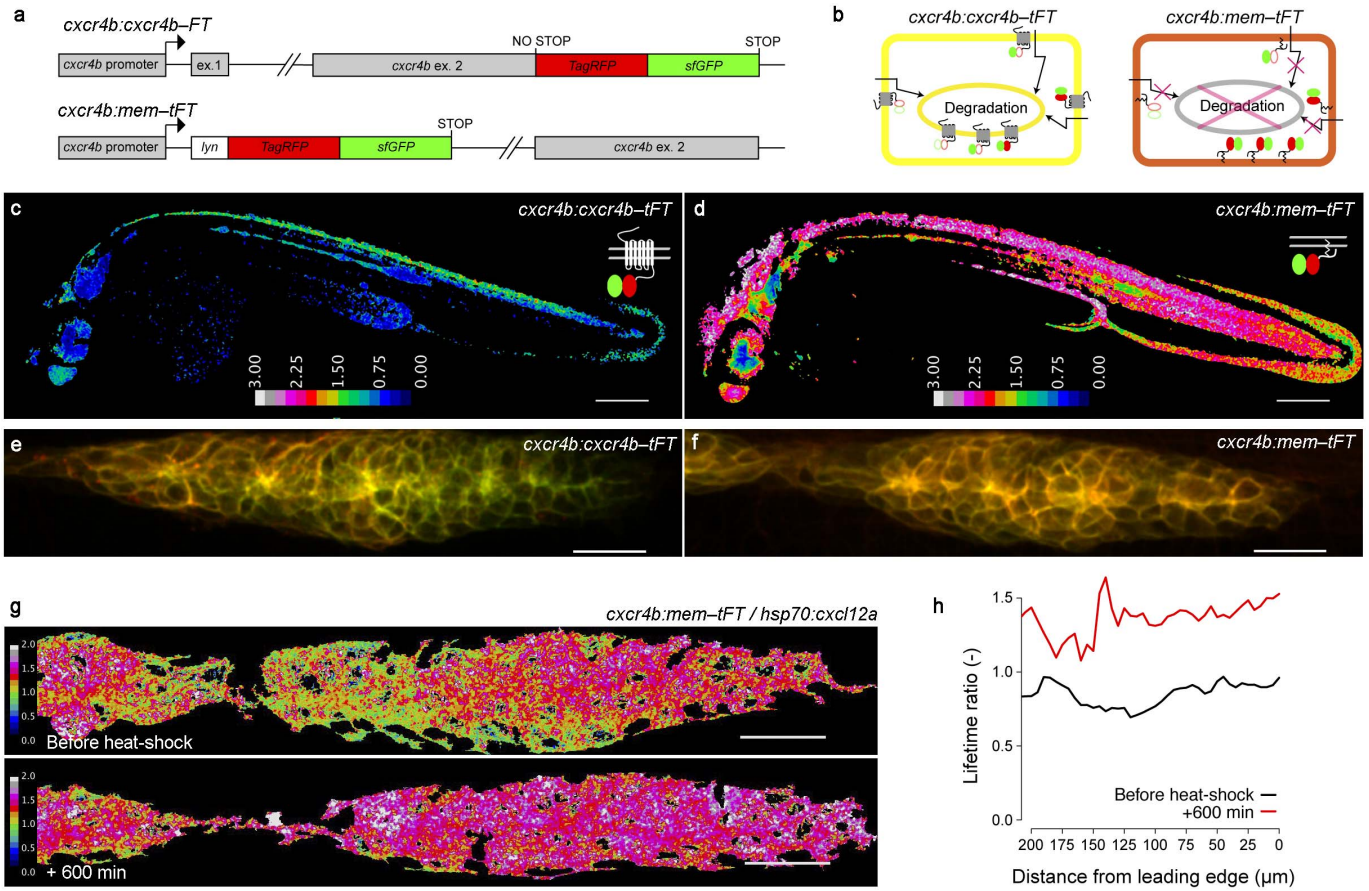

Extended Data Figure 5 | Cxcr4b–tFT lifetime ratio gradient results from protein turnover not from a transcriptional gradient. **a**, Schematic representation of the modified BACs used to create Cxcr4b–tFT and mem-tFT reporter lines. **b**, Predicted behaviour of Cxcr4b–tFT and mem-tFT in response to Cxcl12a. **c**, **d**, Ratiometric images of 36 h.p.f. Cxcr4b–tFT (**c**) and mem-tFT (**d**) of whole-mount transgenic embryos. Segmentation was performed using intensity-based thresholding on sfGFP channel. Scale bars, 200 μm. Calibration bar = normalized red/green ratio. **e**, **f**, Raw primordium images (merge of green and red channels) corresponding to ratiometric images shown in Fig. 2a, b. Scale bars, 20 μm. **g**, Ratiometric images of *cxcr4b:mem-tFT* before (top) and 10 h after (bottom) heat-shock-induced pulse of Cxcl12a. Scale bars, 20 μm. **h**, Spatially resolved lifetime ratio analysis of the sample in **g**. Although overall the ratio increases, during the long time lag, no front to rear gradient could be detected, in contrast to the behaviour of Cxcr4b–tFT (compare to Fig. 2e, f).

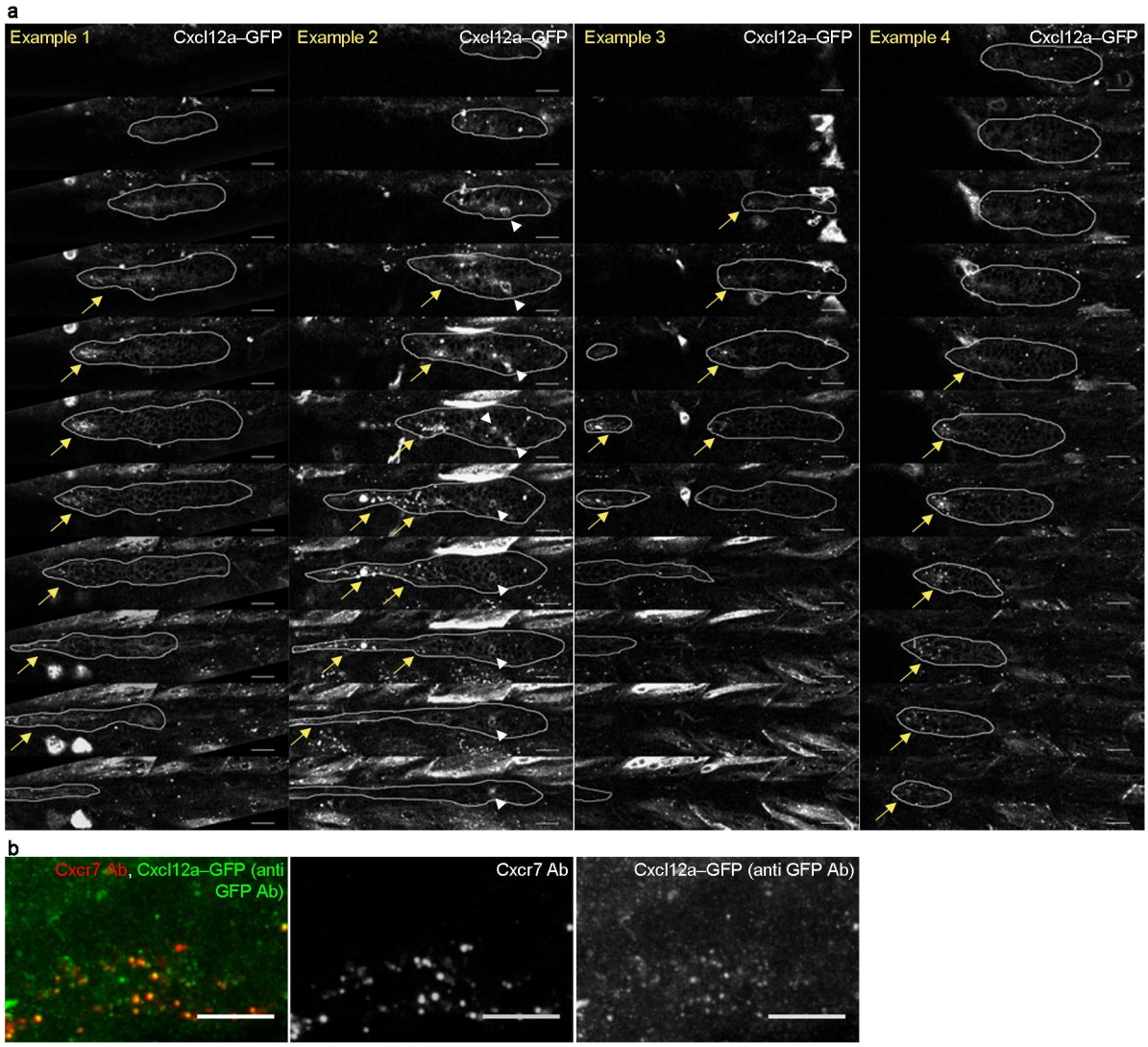

Extended Data Figure 6 | Cxcr7-mediated internalization of Cxcl12a–GFP at the tissue rear. **a**, Film-strip montages of *z*-stacks showing mosaic expression of Cxcl12a–GFP resulting in preferential internalization at the rear of the primordium (outlined by white line, corresponding to Supplementary Video 3). Stacks were acquired 1–2 h after heat-shock induction (1 h at 38 °C) of *hsp70:cxcl12a-GFP_T2A_mKate2-CAAX*-injected embryos. Accumulation of Cxcl12a–GFP-positive vesicles in the primordium (yellow arrows) and Cxcl12a–GFP-expressing cells within the primordium are indicated (white arrowheads). Scale bar, 20 μm. **b**, Anti-GFP and anti-Cxcr7 immunohistochemistry showing co-localization of Cxcl12a–GFP (green) and Cxcr7 (red) in vesicles at the rear of the primordium. Images show maximum intensity projection. Scale bars, 10 μm.

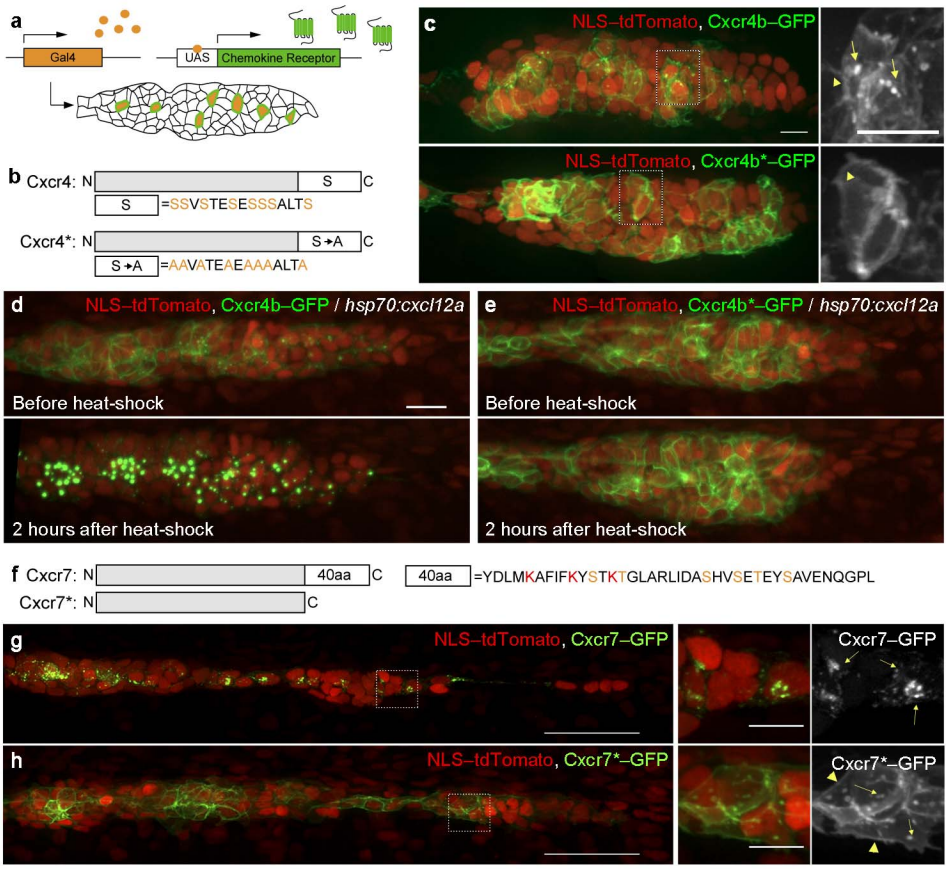

Extended Data Figure 7 | Validation of internalization-defective chemokine receptor forms. **a**, Cartoon illustrating the Gal4/UAS strategy used to induce mosaic expression of chemokine receptors in the primordium. **b**, Schematic of internalization-defective Cxcr4b form (Cxcr4*), as described in ref. 16. Mutated putative phosphorylation sites (S to A) are shown in orange. **c**, Examples of Gal4/UAS-driven expression of Cxcr4b–GFP (green or greyscale, top) or Cxcr4b*–GFP (green or greyscale, bottom) in *cxcr4b:NLS-tdTomato* (red) transgenic embryos. Both receptor forms localize at the plasma membrane (arrowheads). Higher magnification of the squared area shows internalized Cxcr4b (arrows), but not Cxcr4b*, under unstimulated conditions, presumably in response to endogenous Cxcl12a. Scale bars, 10 μm. **d**, **e**, Heat-shock-induced Cxcl12a expression causes complete internalization of Cxcr4b–GFP (**d**), whereas Cxcr4b*–GFP remains at the plasma membrane (**e**). Thus, Cxcr4b* does not internalize Cxcl12a. **f**, An internalization-defective form of Cxcr7 (Cxcr7*) was created by deleting the 40 C-terminal amino acids of the receptor. Putative ubiquitination and phosphorylation target residues, conserved in humans, are shown in red and orange, respectively. **g**, GFP fusion of full-length Cxcr7 localizes in vesicles (arrows in the inset), consistent with antibody stainings of endogenous Cxcr7 (Fig. 3a). **h**, C terminus deletion results in clear receptor re-localization to the plasma membrane (arrowheads). Cxcr7* is only occasionally found in vesicles (arrows). Expression of both receptor forms was driven by Gal4/UAS. Scale bars, 50 μm (10 μm in the insets).

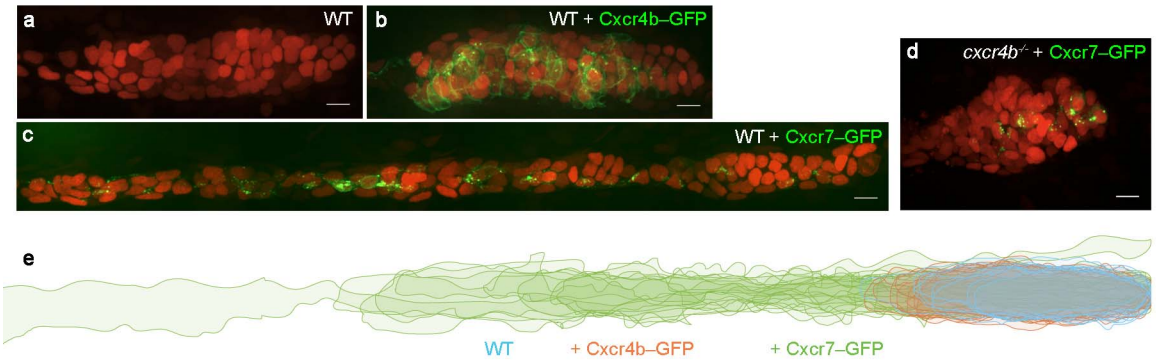

Extended Data Figure 8 | Cxcr7–GFP misexpression alters migrating primordium morphology. **a**–**c**, Primordia at 36 h.p.f. (marked by NLS-dtTomato) in wild type (WT) conditions (**a**) or misexpressing Cxcr4b–GFP (**b**) or Cxcr7–GFP (**c**) under the control of the Gal4/UAS system. **d**, *cxcr4b*$^{-/-}$ primordium misexpressing Cxcr7–GFP (green). Scale bars, 10 μm. **e**, Overlay of outlines of several primordia in the same conditions as in **a**–**c**. Primordia are aligned by the leading edge (right). Ectopic Cxcr7–GFP, but not Cxcr4b–GFP, expression results in primordium elongation. This phenotype is Cxcr4b dependent, as elongated morphology is never observed in Cxcr4b mutants misexpressing Cxcr7–GFP (**d**).

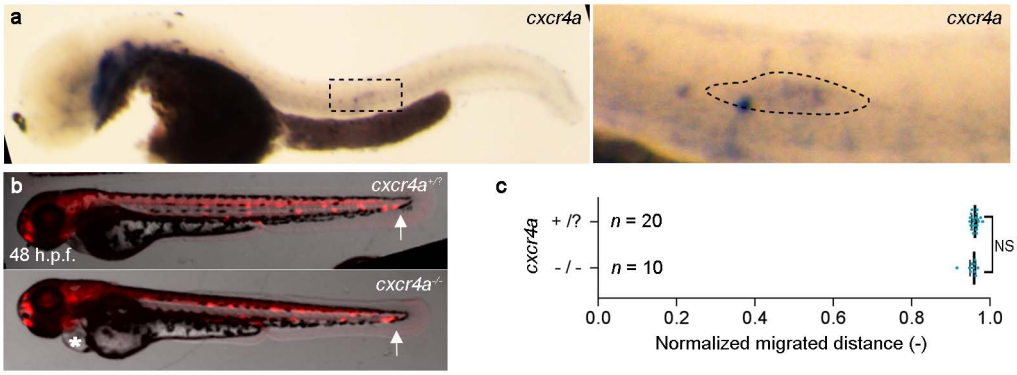

Extended Data Figure 9 | Cxcr4a is not required for primordium migration. **a**, *In situ* hybridization reveals *cxcr4a* expression in the primordium (36 h.p.f. embryo). Inset shows higher magnification of the squared area comprising the primordium. **b**, Images show primordium migration (red = *cxcr4b:NLS-tdTomato*) at 48 h.p.f. in the presence (top) or absence (bottom) of Cxcr4a. Asterisk marks heart oedema, characteristic of $cxcr4a^{-/-}$ (corresponding to $cxcr4a^{um20/um20}$)[32]. **c**, Quantification of primordium migration in $cxcr4a^{-/-}$ embryos. The absence of Cxcr4a does not affect migration when Cxcr4b is present. Dot-plot, median, interquartile range and number of analysed samples are shown. Unpaired *t*-test.

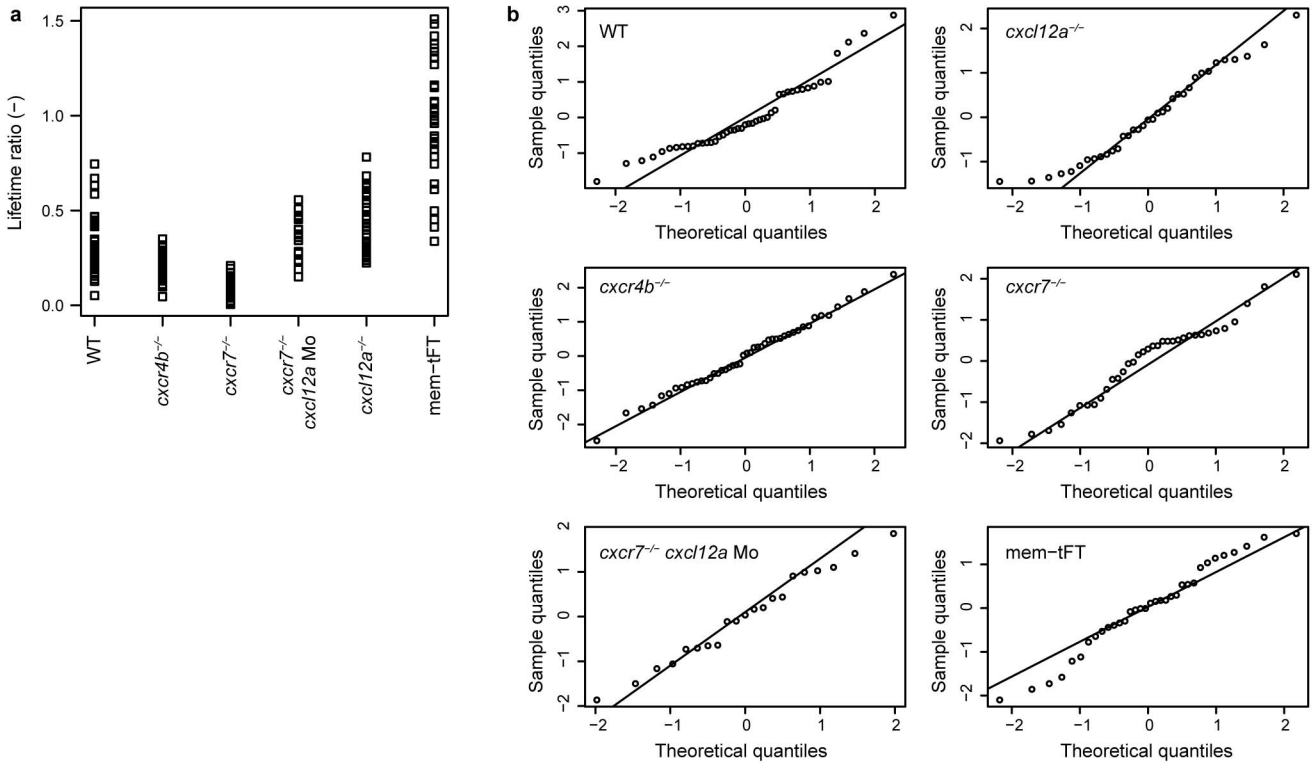

c

					t-test				Mann-Whitney test	
cond1	cond2	mean1	mean2	difference in means	t	df	p.value	p.adjusted (Bonferroni)	W	p.value
WT	mem-tFT	0.318	0.984	0.666	-11.643	44.597	4.10E-15	2.46E-14	45	4.27E-17
WT	*cxcl12a*$^{-/-}$	0.318	0.439	0.121	-3.600	73.091	5.77E-04	3.46E-03	419	2.70E-04
WT	*cxcr4b*$^{-/-}$	0.318	0.201	-0.118	4.907	58.858	7.66E-06	4.60E-05	1583	7.59E-06
WT	*cxcr7*$^{-/-}$	0.318	0.103	-0.215	9.080	56.462	1.24E-12	7.47E-12	1515	2.28E-16
cxcr7$^{-/-}$	*cxcr7*$^{-/-}$ *cxcl12a* Mo	0.103	0.354	0.251	-9.901	25.211	3.59E-10	2.15E-09	6	4.46E-14
cxcr7$^{-/-}$	*cxcr4b*$^{-/-}$	0.103	0.201	0.098	-7.779	78.680	2.40E-11	1.44E-10	163	2.18E-11

Extended Data Figure 10 | Statistical analysis of tissue-scale lifetime ratios. **a**, Summary of tissue-scale lifetime ratio distributions at 32 h.p.f. (data corresponding to Figs 2d and 3c). **b**, Quantile-quantile (Q-Q) plots of the analysed data sets. **c**, Statistical tests results.